

EFFECTS OF INTERNAL DYNAMICS ON CHEMOTACTIC AGGREGATION OF BACTERIA

SHUGO YASUDA

ABSTRACT. Effects of the internal adaptation dynamics on the self-organized aggregation of chemotactic bacteria are investigated by Monte Carlo (MC) simulations based on a two-stream kinetic transport equation coupled with a reaction-diffusion equation of the chemoattractant that bacteria produce.

A remarkable finding is a nonmonotonic behavior of the peak aggregation density with respect to the adaptation time; more specifically, the aggregation is the most enhanced when the adaptation time is moderately larger than the mean run time of bacteria.

Another curious observation is the formation of a trapezoidal aggregation profile occurring at a very large adaptation time, where the biased motion of individual cells is rather hindered at the plateau regimes due to the boundedness of the tumbling frequency modulation.

The asymptotic behavior of the MC results further reveals that the trapezoidal aggregation is robustly formed for the bacteria with a stiff chemotactic response when the adaptation time is as large as the diffusion time of the macroscopic population density and that the classical Keller-Segel model, which is derived from the kinetic transport model in the continuum limit, is only valid when the adaptation time is much smaller than the diffusion time.

1. INTRODUCTION

The collective motion of chemotactic bacteria, such as *Escherichia coli*, stems from, at the individual level, continuous reorientation via runs and tumbles. It has been established that the length of a run is determined by a stiff response to the temporal variation of extracellular chemical cues via an intracellular signal transduction pathway. The chemotactic response and the intracellular signal transduction pathway for *E. coli* have been extensively studied by various authors, and sophisticated mathematical models have been proposed. [12, 16, 31] However, the multiscale mechanism between the intracellular signal transduction, individual chemotactic motion, and collective dynamics of cells is not well understood yet. Nowadays, engineered bacteria (or genetically modified bacteria) are utilized in a variety of industrial fields involving, for example, food, agriculture, medicine, and environment. Understanding of the multiscale mechanism can contribute to further advance the industrial technology to control the collective motion of cells.

Kinetic transport models have been proposed to describe the multiscale mechanism in the collective motion of cells; a kinetic transport model describing the velocity jump process in the run-and-tumble motion of *E. Coli* was first proposed in Ref. [19], and it was then further developed towards involving more detailed chemosensory systems [7, 8, 26]. Although the chemosensory system involves complicated biochemical reaction pathways, in the simplified description, it can be constituted by two essential steps, i.e., a rapid response to an external signal change called “excitation” and a subsequent slow “adaptation”, in which the internal state returns to the baseline, allowing the cell to respond to a further external signal change.[28] A kinetic transport equation involving the simplified description of the excitation and adaptation dynamics has been proposed in Refs. [8] and [9], where two internal state variables are introduced in the model. Since the

Date: March 13, 2022.

Key words and phrases. chemotaxis; aggregation; instability; kinetic transport equation; Monte Carlo simulation.

This work was supported by Japan-France Integrated action program (SAKURA), Grant number JPJSBP120193219.

excitation dynamics are much faster than the adaptation dynamics, one can integrate out the fast variable related to the excitation and derive the kinetic transport equation involving only a single internal state variable related to the slow adaptation dynamics[26], i.e.,

$$\partial_t p + \mathbf{v} \cdot \nabla_x p + \partial_m [F(m, S)p] = \mathcal{Q}[m, S](p), \quad (1)$$

where $p(t, \mathbf{x}, \mathbf{v}, m)$ is the density of cells with velocity $\mathbf{v} \in \mathbb{V}$ and internal state $m > 0$ at time $t > 0$ and position $\mathbf{x} \in \mathbb{R}^d$. Here, on the left-hand side, the x -divergence term describes the change in density due to the “run” of the bacteria, and the m -derivative term describes the evolution of the internal state m at the rate of change $F(m, S)$, where $S(t, \mathbf{x})$ is the concentration of the extracellular chemical cue. On the right-hand side, $\mathcal{Q}[y, S](p)$ is the tumbling operator described as

$$\mathcal{Q}[m, S](q) = \frac{1}{\|\mathbb{V}\|} \int_{\mathbb{V}} [\lambda(m, S, \mathbf{v}, \mathbf{v}') p(t, \mathbf{x}, \mathbf{v}', m) - \lambda(m, S, \mathbf{v}', \mathbf{v}) p(t, \mathbf{x}, \mathbf{v}, m)] d\mathbf{v}', \quad (2)$$

where $\lambda(m, S, \mathbf{v}, \mathbf{v}')$ denotes the tumbling frequency describing the reorientation from velocity \mathbf{v}' to the new velocity \mathbf{v} . The velocity space \mathbb{V} is the bounded domain of \mathbb{R}^d and $\|\mathbb{V}\| = \int_V dv$.

Since the bacteria communicate with each other via the extracellular chemical cues they produce, to describe the self-organization phenomena occurring in a population of chemotactic bacteria as observed, for example, in Refs. [5, 18, 33], chemoattractant equations must be coupled with the kinetic transport model (1). In this study, we consider a single species of chemical cue whose concentration $S(t, \mathbf{x})$ is described as

$$\partial_t S = D_S \Delta S - aS + b\rho, \quad (3)$$

where D_S is the diffusion coefficient of the chemical cue, a is the degradation rate of the chemical cue, b is the production rate of the chemical cue by bacteria, and $\rho(t, \mathbf{x}) = \int_{\mathbb{V}} \int_0^\infty p(t, \mathbf{x}, \mathbf{v}, m) dm d\mathbf{v}$ is the population density of bacteria.

In the kinetic transport model, the microscopic characteristics at the individual level are involved in the tumbling frequency $\lambda(m, S, \mathbf{v}, \mathbf{v}')$ and the rate of change of the internal state $F(m, S)$. Thus, by specifying the mathematical formulas for $\lambda(m, S, \mathbf{v}, \mathbf{v}')$ and $F(m, S)$, one can address the multiscale mechanism between the intracellular adaptation dynamics, individual chemotactic motion, and collective dynamics of cells in the self-organization phenomena. One can also derive macroscopic models for the population density of bacteria, e.g., Keller-Segel (KS)-type systems [10, 14, 15], and kinetic transport equations without internal state variables [7] by using moment closure or asymptotic analysis of Eqs. (1)–(3). [21, 22, 29, 34]

Investigations of the aggregation of chemotactic bacteria based on kinetic transport models have been carried out in various studies. For example, in Ref. [27], the aggregation of chemotactic bacteria under a given concentration gradient of a chemical cue is investigated based on the kinetic transport model with internal states, and the volcano-like (bimodal) aggregation of *E. coli* observed in an experiment [18] was numerically reproduced in one-dimensional space. In Ref. [35], the concentric stripe patterns formed by engineered *E. coli*[17] were reproduced numerically, and the role of intracellular signal transduction in stripe pattern formation was clarified. In Ref. [23], the instability of the kinetic transport model describing colony pattern formation over a long period of time due to proliferation was investigated, and stiff-response-induced instability was uncovered at the kinetic level. Additionally, in Ref. [25], the role of the hydrodynamic interaction in the self-organized aggregations was numerically investigated by using a Monte Carlo method related to a kinetic transport model without internal states. These studies have proven that kinetic transport models are useful for elucidating the multiscale mechanism in the collective motion of chemotactic bacteria. However, the instability conditions under which aggregations autonomously form in a rather short period of time without proliferation and the role of the internal dynamics in the self-organized aggregations have yet to be clarified.

In this paper, we investigate the self-organized aggregations of chemotactic bacteria in one-dimensional space based on a two-stream kinetic transport model with an internal state. In contrast to a previous study [23], we consider the aggregation of chemotactic bacteria, which may be formed in a rather short period of time without proliferation, and numerically investigate the instability and aggregation in the kinetic transport equation with an internal state coupled with the chemoattractant equation. In particular, we focus on the effect of the adaptation time on the instability and aggregation behavior.

In the following text, the problem and the basic equations are given in Sec. 2. In Sec. 3, numerical analyses are carried out for a wide range of adaptation times by using a Monte Carlo (MC) method, which is an extension of the MC method previously developed in Refs. [32, 36]. Here, a variety of aggregation profiles are uncovered from both microscopic and macroscopic points of view as well as instability diagrams. In Sec. 4, we formally carry out the asymptotic analysis of the kinetic transport model at different scalings of the adaptation time and derive a related KS model. The asymptotic behavior is also numerically investigated over a wide range of adaptation times, through which a suitable parameter regime for the KS system is uncovered and a remarkable numerical solution obtained at a very large adaptation time, which may indicate a novel type of asymptotic solution. Finally, a summary and perspectives are given in Sec. 5.

2. PROBLEM AND FORMULATION

We consider the chemotactic bacteria moving in positive and negative directions with a constant speed V_0 , i.e., $v = \{-V_0, V_0\}$, in one-dimensional space $x \in [0, L]$ with periodic boundary conditions. Initially, the bacteria are uniformly distributed, and the internal state m is in the equilibrium state at $m = M(S)$, where $M(S)$ denotes the equilibrium internal state determined by the extracellular chemical concentration. The chemical concentration $S(t, x)$ is also uniformly distributed in the initial state.

For the internal state dynamics, we consider the following linear adaptation model:

$$\frac{dm}{dt} = F(m, S) = \frac{M(S) - m}{\tau}, \quad (4)$$

where $\tau > 0$ denotes the characteristic adaptation time. We also assume that the bacteria tumble (i.e., change moving direction) depending only on the deviation of the internal state m from the equilibrium state $M(S)$, $M(S) - m$, [26]:

$$\lambda(m, S, v, v') = \lambda_0 \Lambda \left(\frac{M(S) - m}{\delta} \right), \quad (5)$$

where $\lambda_0 > 0$ is the mean tumbling frequency, $\Lambda \left(\frac{M(S) - m}{\delta} \right) > 0$ denotes the modulation of the tumbling frequency, and $\delta > 0$ denotes the stiffness of the chemotactic response. In this study, we consider the following modulation function:

$$\Lambda_\delta(y) = \Lambda \left(\frac{y}{\delta} \right), \quad \Lambda(y) = 1 - R(y), \quad R(y) = \frac{\chi y}{\sqrt{1 + y^2}}, \quad (6)$$

where $0 < \chi < 1$ denotes the modulation amplitude and δ denotes the stiffness of the chemotactic response.

Then, the density of bacteria with positive and negative velocities, $p^\pm(t, x, m)$, are described by the two-stream kinetic transport equation with the internal state,

$$\partial_t p^\pm \pm V_0 \partial_x p^\pm + \partial_m \left(\frac{M(S) - m}{\tau} p^\pm \right) = \pm \frac{\lambda_0}{2} \Lambda_\delta(M(S) - m) (p^- - p^+). \quad (7)$$

By introducing the nondimensional variables

$$\hat{x} = x/L_0, \quad \hat{t} = t/t_0, \quad \hat{v} = v/V_0,$$

where L_0 , V_0 , and t_0 are the characteristic length, speed, and time, respectively, Eq. (7) is written in nondimensional form as

$$\hat{\sigma}\partial_{\hat{t}}\hat{p}^{\pm} \pm \partial_{\hat{x}}\hat{p}^{\pm} + \partial_m \left(\frac{M(S) - m}{\hat{\tau}} p^{\pm} \right) = \frac{\hat{\lambda}_0}{2} \Lambda_{\delta}(M(S) - m) (\hat{p}^{\mp} - \hat{p}^{\pm}). \quad (8)$$

Here, the nondimensional parameters $\hat{\sigma}$, $\hat{\lambda}_0$, and $\hat{\tau}$ are defined as

$$\hat{\sigma} = L_0/(t_0 V_0), \quad \hat{\lambda}_0 = \lambda_0/(V_0/L_0), \quad \hat{\tau} = \tau/(L_0/V_0). \quad (9)$$

We also define $\hat{p}^{\pm} = p^{\pm}/\rho_0$, where ρ_0 is the initial population density of bacteria. By the same token, the nondimensional form of (3) is written as

$$\hat{\sigma}_S \partial_{\hat{t}} \hat{S} = \hat{D}_S \partial_{\hat{x}} \hat{S} - \hat{S} + \hat{\rho}, \quad (10)$$

where the nondimensional quantities are defined as

$$\hat{\sigma}_S = 1/(at_0), \quad \hat{D}_S = D_S/(aL_0^2), \quad \hat{S} = S/(b\rho_0/a), \quad \hat{\rho} = \rho/\rho_0, \quad (11)$$

and the population density $\hat{\rho}$ is calculated as

$$\hat{\rho}(x, t) = \int_0^{\infty} \frac{\hat{p}^+(t, x, m) + \hat{p}^-(t, x, m)}{2} dm. \quad (12)$$

In the rest of the paper, unless otherwise stated, all quantities are written in nondimensional forms, and we drop the hat signs on the variables and parameters for simplicity.

It is convenient to introduce the new internal state variable $y = M(S) - m \in \mathbb{R}$ and change the variable as $f^{\pm}(t, x, y = M(S) - m) = p^{\pm}(t, x, m)$. Then, we obtain

$$\sigma \partial_t f^{\pm} \pm \partial_x f^{\pm} + \partial_y \left\{ \left(D_t^{\pm} M(S) - \frac{y}{\tau} \right) f^{\pm} \right\} = \pm \frac{\lambda_0 \Lambda_{\delta}(y)}{2} (f^{-} - f^{+}), \quad (13)$$

where D_t^{\pm} denotes the material derivative defined as $D_t^{\pm} = \sigma \partial_t \pm \partial_x$. Here, the y -derivative term of (13) describes the change in the internal state variable y , where $D_t^{\pm} M(S)$ denotes the temporal variation of the extracellular chemical cue sensed by moving bacteria at the first step in the intracellular signal transduction pathway. Since *E. coli* cells respond to the spatial gradient of the logarithmic extracellular chemical concentration[3, 13], we model the logarithmic sensing by

$$D_t^{\pm} M(S) = D_t^{\pm} \ln S(x, t) = \frac{\sigma \partial_t S \pm \partial_x S}{S}. \quad (14)$$

It can be clearly seen that the uniform state $f^{\pm} = \delta(y = 0)$ and $S = \rho = 1$, where $\delta(y)$ is the Dirac delta function, solves the system of Eqs. (10) and (13). We investigate the instability of the uniform state by the Monte Carlo code explained in Sec. 3.1. This study is an extension of a previous study[23], where we investigated the instability of a different type of kinetic transport equation, which can be derived from Eq. (13) when the adaptation is very fast, as $\tau \ll \lambda_0^{-1}$ [21], and uncovered that the stiffness of the response, i.e., the parameter χ/δ , is the key factor to induce instability. In this study, we focus on the effect of the adaptation time τ on the instability and aggregation behavior.

3. NUMERICAL ANALYSIS

3.1. Monte Carlo method. The one-dimensional space $0 \leq x \leq L$ is divided into the uniform mesh system $x_i = \Delta x \times i$ ($i = 0, \dots, I$) with the mesh width $\Delta x = L/I$, where I is the number of mesh intervals. Initially, Monte Carlo (MC) particles are uniformly distributed in each mesh interval with the equilibrium interval state at $y = 0$. The velocities of each MC particle, $v = \pm 1$, are randomly determined. The chemical concentrations in each mesh interval $x \in [x_i, x_{i+1}]$ ($i = 0, \dots, I - 1$), S_i are also uniformly given at the initial state, i.e., $S_i^0 = 1$.

Then, the position r_l^k , velocity v_l^k , internal state y_l^k of the l th MC particle at time $t = k\Delta t$ are determined as following,

- (1) Each MC particle moves as

$$r_l^k = r_l^{k-1} + v_l^{k-1}\Delta t. \quad (15)$$

- (2) Population density in the i th mesh interval $x \in [x_i, x_{i+1}]$, ρ_i^k is calculated as

$$\rho_i^k = \frac{1}{\bar{N}} \sum_{l=0}^N \int_{x_i}^{x_{i+1}} \delta(x - r_l^k) dx, \quad (16)$$

where \bar{N} is the number of MC particles in each mesh interval at the uniform state. Thus, the total number of MC particle is given by $I \times \bar{N}$.

- (3) Concentration of chemical cue in the i th mesh interval, S_i^k is calculated explicitly as,

$$\sigma_S \frac{S_i^k - S_i^{k-1}}{\Delta t} = \frac{D_S}{\Delta x^2} (S_{i+1}^{k-1} - 2S_i^{k-1} + S_{i-1}^{k-1}) - S_i^{k-1} + \rho_i^k. \quad (17)$$

At the boundaries $x=0$ and L , we consider the periodic condition, i.e., $S_{-1} = S_{I-1}$ and $S_I = S_0$.

- (4) Internal state of the l th MC particle, y_l^k is updated as

$$\frac{y_l^k - y_l^{k-1}}{\Delta t} = \frac{S^k(x = r_l^k) - S^{k-1}(x = r_l^{k-1})}{\Delta t} - \frac{y_l^k}{\tau}, \quad (18)$$

where $S^k(x = r_l^k)$ denotes the local concentration of chemical cue at $x = r_l^k$ and is calculated by the linear interpolation,

$$S^k(x = r_l^k) = \begin{cases} S_i^k + \frac{S_i^k - S_{i-1}^k}{\Delta x} (r_l^k - x_i - \frac{\Delta x}{2}), & \text{if } x_i \leq r_l^k < x_i + \frac{\Delta x}{2}, \\ S_i^k + \frac{S_{i+1}^k - S_i^k}{\Delta x} (r_l^k - x_i - \frac{\Delta x}{2}), & \text{if } x_i + \frac{\Delta x}{2} \leq r_l^k < x_{i+1}. \end{cases} \quad (19)$$

- (5) Tumbling of the l th MC particle is decided by the probability $\frac{\Delta t \lambda_0}{2} \Lambda_\delta(y_l^k)$.

- (6) The particles which are decided to make tumble change their velocities as $v_l^k \rightarrow -v_l^{k-1}$, other particles remain their velocities.

This MC method was applied for the aggregation under a given constant spatial-gradient of chemical cue, i.e., $\partial_x M(S) = \text{const.}$, in Ref. [32] and the accuracy of the MC method was confirmed throughout the comparison to the asymptotic preserving schemes developed in the paper.

3.2. Numerical results. The MC simulations are performed for various values of the mean tumbling frequency λ_0 , the adaptation time τ , and the stiffness of the chemotactic response δ while the diffusion constant $D_S = 1$, the length of the periodic interval $L = 10$, the modulation amplitude $\chi = 0.5$, and the time scale parameters $\sigma = \sigma_S = 1$ are fixed. Here, we also introduce a new parameter α , which is defined by the ratio of the adaptation time τ to the mean run time λ_0^{-1} , i.e., $\alpha = \lambda_0 \tau$, and call it the relative adaptation time. The number of mesh interval $I=50$ and the average number of MC particles in each mesh interval $\bar{N}=28,800$ are used except the cases for $\lambda_0=500$ and 1000 at $\delta = 0.01$, where $I = 100$ and $\bar{N} = 7,400$ are used. The time step size is set as $\Delta t = 10^{-3}$ for $\lambda_0 < 100$, $\Delta t = 2 \times 10^{-4}$ for $\lambda_0=100$ and 200 , and $\Delta t = 5 \times 10^{-5}$ for $\lambda_0 = 500$ and 1000 .

3.2.1. Instability and aggregation profile. Figures 1 and 2 show the time evolutions of the population density of bacteria at different values of the relative adaptation time α . Figure 1 shows the result at the moderate stiffness $\delta = 0.1$ while Figure 2 shows that at the large stiffness $\delta = 0.01$. In both figures, the tumbling frequency $\lambda_0 = 10$ is fixed. Initially, the population density ρ is uniformly distributed with small fluctuations, whose amplitudes are at most 0.015.

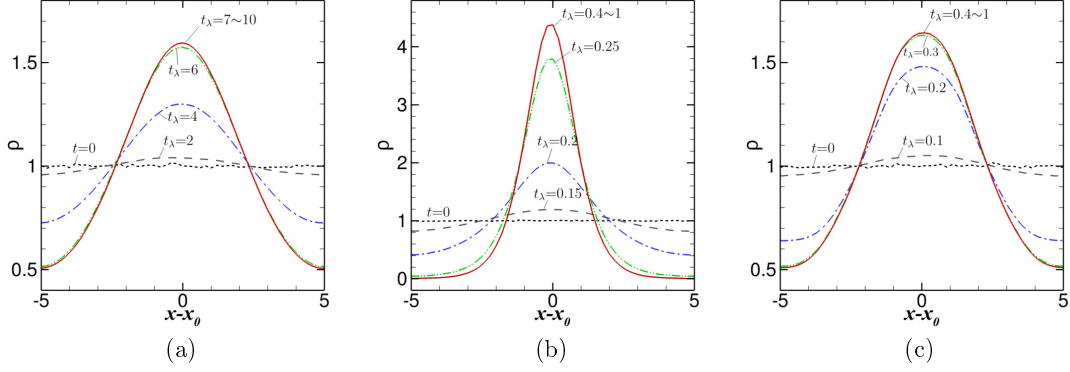


FIGURE 1. Time evolutions of the population density of bacteria with the moderate stiffness $\delta = 0.1$ at different values of the relative adaptation time, i.e., $\alpha = 0.4$ (a), $\alpha = 1$ (b), and $\alpha = 100$ (c), at the mean tumbling frequency $\lambda_0 = 10$. Here, x_0 represents the position where the chemical cue S takes the maximum value in the stationary state and t_λ is defined as $t_\lambda = t/(\lambda_0 L^2)$. In each figure, the MC results, except for those at $t = 0$, are time-averaged over the small time interval $t_\lambda = 0.05$ in order to remove the fluctuations caused by the Monte Carlo method while the result at $t = 0$ shows the snapshot of the initial uniform state, which involves small fluctuations.

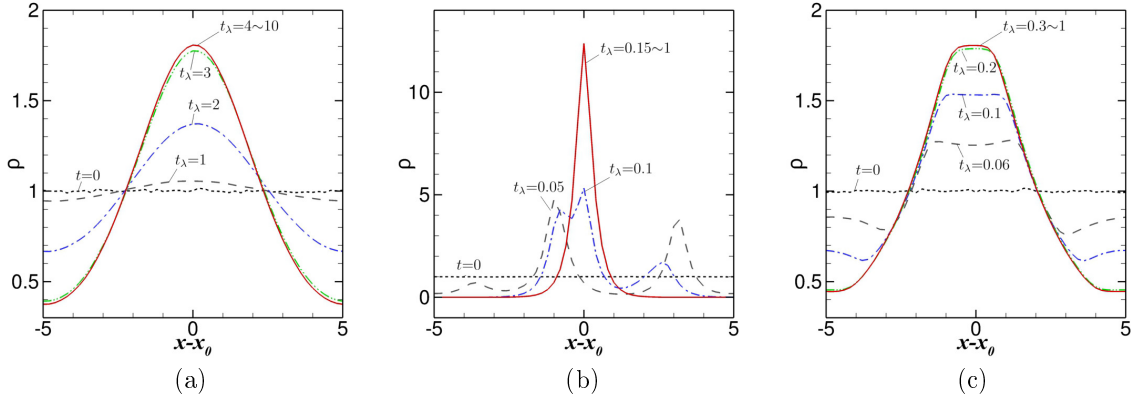


FIGURE 2. Time evolutions of the population density of bacteria with the large stiffness $\delta = 0.01$ at different values of the relative adaptation time, i.e., $\alpha = 0.03$ (a), $\alpha = 1$ (b), and $\alpha = 100$ (c), at the mean tumbling frequency $\lambda_0 = 10$. See also the caption in Fig. 1.

The aggregation profiles are highly affected by the adaptation time and the stiffness. At the moderate stiffness $\delta = 0.1$ (Fig. 1), the sinusoidal-like curves are generated in the stationary states at small and large adaptation times, i.e., $\alpha = 0.4$ and 100, while at $\alpha = 1$, a sharp aggregation profile is generated in the stationary state.

At the large stiffness $\delta = 0.01$ (i.e., Fig. 2), a very sharp aggregation, i.e., the spike-like aggregation profile is formed at $\alpha = 1$ in the stationary state. On the other hand, interestingly, at the large adaptation time $\alpha = 100$ (see Fig. 2(c)), the aggregation is not enhanced but is rather hindered at the central region of the aggregation profile such that the trapezoidal profile, where the plateau regimes appear at the top and bottom of the aggregation, is formed. Later on, we will see that this remarkable profile is obtained at the large stiffness when the adaptation time is so large as $\tau = O(\lambda_0)$.

It should be remarked that in both Figs. 1 and 2, the maximum aggregation density is not monotonically dependent on the adaptation time; the aggregation is enhanced at the moderate relative adaptation time $\alpha = 1$. The nonmonotonic dependency of the maximum aggregation density on the adaptation time is discussed at Fig. 4.

The spatial profiles of chemical cue S are shown in Fig. 7(c). In contrast to the population density of bacteria ρ , the spatial distribution of S is moderate and not significantly affected by either the relative adaptation time α and the stiffness δ .

It is also seen that the time evolution is much slower at the small relative adaptation time (Figs. 1(a) and 2(a)) than other cases although the sinusoidal-like profile is clearly formed in the stationary state. This indicates that the parameter sets used in Fig. 1(a) and Fig. 2(a) are close to the critical regime for the instability of the uniform state. In fact, as is seen in Fig. 3(b), the parameter sets used in Fig. 1(a) and Fig. 2(a) are located in the vicinity of, but slightly above the linear stability condition of the KS system given in Sec. 4.

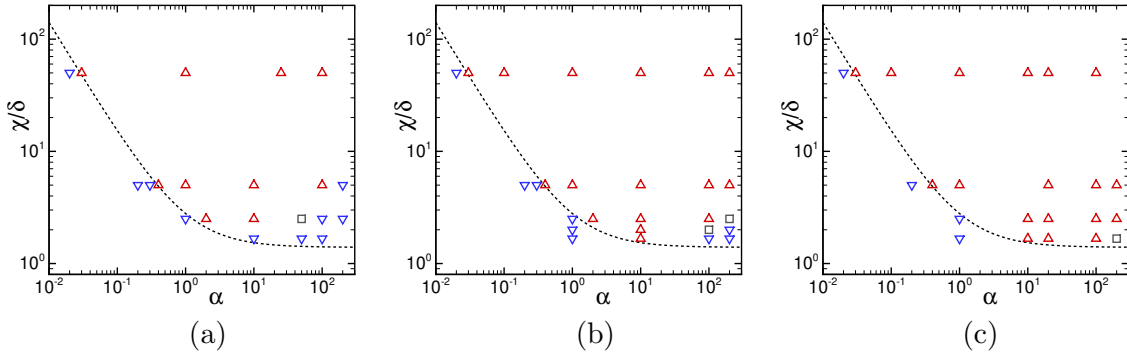


FIGURE 3. The instability diagrams with respect to the scaled adaptation time α and the stiffness χ/δ at $\lambda_0 = 5$ (a), $\lambda_0 = 10$ (b) and $\lambda_0 = 20$ (c). The upward triangles Δ show the results where stationary patterns are clearly observed while the downward triangles ∇ show the results where no evident patterns are observed (where the maximum difference of the population density from the uniform state, $\Delta\rho = \rho_{\max} - 1$ is less than 0.01). See also Fig. 4. The squares \square show the intermediate results where non-stationary sinusoidal waves with small amplitudes, i.e., $0.01 < \Delta\rho < 0.1$, are observed. The dotted line shows the linear stability condition of the KS system, which is obtained in Sec. 4.2. Under the critical line, the uniform solution of the KS system is linearly stable.

Figure 3 shows the instability diagrams with respect to the relative adaptation time α and the stiffness of the chemotactic response χ/δ at different values of the tumbling frequency, i.e., $\lambda_0 = 5$ in (a), $\lambda_0 = 10$ in (b), and $\lambda_0 = 20$ in (c). It is clearly seen that when the relative adaptation time α is fixed, the instability occurs when the stiffness χ/δ is sufficiently large. At small relative adaptation times, say $\alpha \lesssim 1$, the critical values of the relative adaptation time α for the instability are always consistent with the linear stability condition of the KS system, and the transition between the stable and unstable regimes is very sharp.

It is also seen that the critical behavior for the instability is not so affected by the mean tumbling frequency λ_0 in the small α regime. However, at the large α regime, say $\alpha \gtrsim 10$, the instability behavior is significantly affected by the mean tumbling frequency λ_0 , and the instability condition of the KS system is no more consistent with the MC results especially at $\lambda_0 = 5$ (Fig. 3(a)).

The nonmonotonic behavior of the maximum aggregation density with respect to the relative adaptation time is seen in Figure 4. It is clearly seen that the transition from the stable to unstable modes is very sharp

at the small α regime, say $\alpha \lesssim 1$. On the other hand, at the large α regime, the maximum aggregation density gradually decreases as α increases, and the slope of the decrease is larger as λ_0 is smaller. This behavior is completely different from that in the KS system, where the maximum aggregation density monotonically increases and saturates to a certain value as the relative adaptation time α increases. It should be remarked that at any fixed λ_0 , there exist the optimal adaptation time to enhance the aggregation in the regime $1 < \alpha \ll \lambda_0$. Importantly, this nonmonotonic behavior is a distinguished result obtained by the kinetic system but not by the KS system.

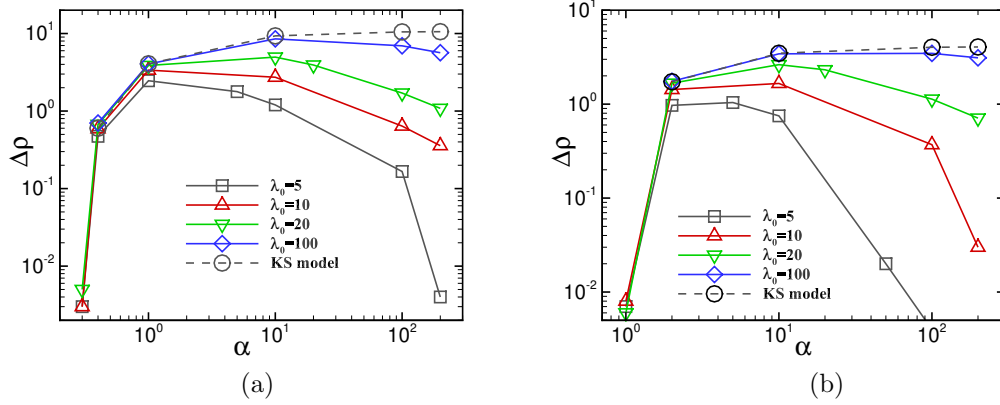


FIGURE 4. The dependency of the maximum aggregation density on the relative adaptation time α at different values of the mean tumbling frequency λ_0 . Figure (a) shows the result at $\delta = 0.1$ and Figure (b) shows the result at $\delta = 0.2$. Here, the vertical axis shows the difference between the maximum aggregation density ρ_{\max} and the uniform state $\rho = 1$, i.e., $\Delta\rho = \rho_{\max} - 1$. The results of the KS system are obtained by the numerical computation with the finite difference scheme on the staggered grid given in Ref. [6].

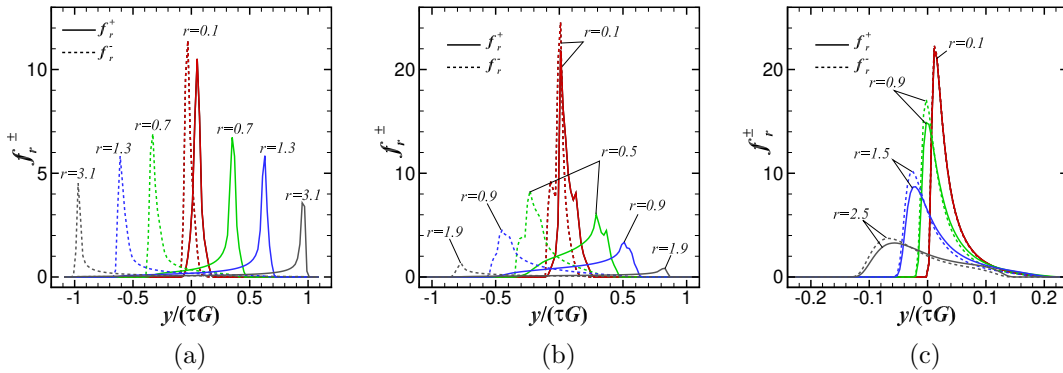


FIGURE 5. The stationary distributions of the internal state y at different distances from the center of the aggregation $r = |x - x_0|$ at the moderate stiffness $\delta = 0.1$. Figures (a), (b), and (c) show the results at different relative adaptation times, i.e., $\alpha = 0.4$, $\alpha = 1$, and $\alpha = 100$, respectively, at the mean tumbling frequency $\lambda_0 = 10$. Here, G denotes the maximum value of the spatial gradient of $M(S)$, i.e., $G = \max_x |\partial_x M(S)|$.

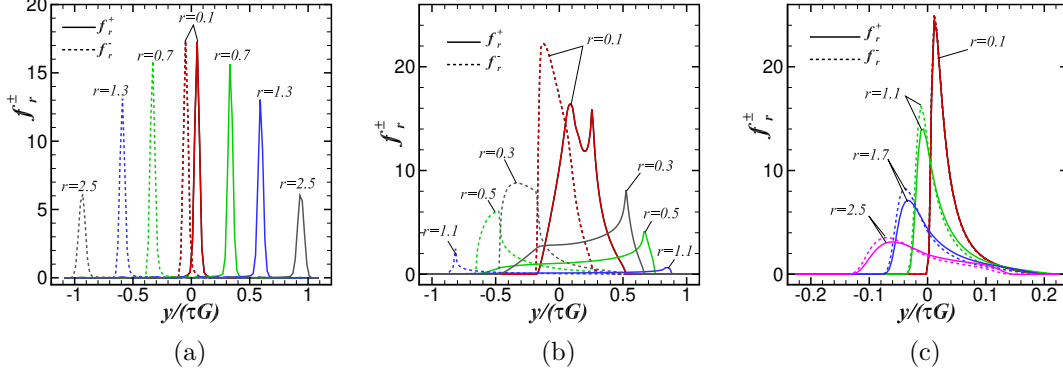


FIGURE 6. The stationary distributions of the internal state y at different distances from the center of the aggregation $r = |x - x_0|$ at the large stiffness $\delta = 0.01$. Figures (a), (b), and (c) show the results at different relative adaptation times, i.e., $\alpha = 0.03$, $\alpha = 1$, and $\alpha = 100$, respectively, at the mean tumbling frequency $\lambda_0 = 10$. See also the caption in Fig. 5.

3.2.2. *Distribution of the internal state.* Figure 5 and 6 show the stationary distributions of the internal state y at different distances from the center of the aggregation $r = |x - x_0|$, which are defined as

$$f_r^\pm(y) = \frac{f^+(x_0 \mp r, y) + f^-(x_0 \pm r, y)}{2}.$$

That is, $f_r^\pm(y)$ denote the local distributions of internal state y for the bacterial moving, respectively, toward and outward the maximum aggregation density at the distance r from the center of the aggregation. Figure 5 shows the result at the moderate stiffness $\delta = 0.1$ while Fig. 6 shows that at the large stiffness $\delta = 0.01$. The parameter sets used in Figs. 5 and 6 are same in Figs. 1 and 2, respectively.

It is seen that the distribution of internal state is highly affected by the relative adaptation time. When the relative adaptation time is small (i.e., Figs. 5(a) and 6(a)), f_r^+ and f_r^- are symmetric to each other with respect to $y = 0$ and have steep peaks at different values of the internal state according to the distance r . Table 1 shows the relation between the peak position of $f_r^\pm(y)$ with respect to y , say y_p^\pm , and the local spatial gradient of $M(S)$ at the distance r . It is seen that the following relation almost holds at each distance r , i.e.,

$$y_p^\pm = \pm\tau|\partial_x M(S)|.$$

r	Fig. 5(a)			Fig. 6(a)		
	$y_p^+ / (\tau G)$	$y_p^- / (\tau G)$	$ \partial_x M/G $	$y_p^+ / (\tau G)$	$y_p^- / (\tau G)$	$ \partial_x M/G $
0.1	0.05	-0.03	0.07	0.05	0.05	0.05
0.7	0.35	-0.33	0.37	0.33	0.33	0.35
1.3	0.63	-0.61	0.63	0.59	0.59	0.62
2.5	0.97	-0.95	0.99	0.93	0.93	0.97

TABLE 1. Relation between the peak positions of $f_r^\pm(y)$ with respect to y , y_p^\pm in Fig. 5(a) and Fig. 6(a) and the local spatial gradient of $M(S)$. See also the caption in Fig. 5.

This behavior is intuitively explained as following. From Eq. (4) and the definition of y , the dynamics of the internal state y of each bacterium is described as

$$\dot{y} = \dot{M}(S) - \frac{y}{\tau},$$

where $\dot{M}(S)$ is the temporal derivative of $M(S)$ along the moving path of each bacterium and is replaced with $|\partial_x M(S)|$ (or $-|\partial_x M(S)|$) at each local position r when the bacteria moves toward (or outward) the maximum aggregation density. Note that $\dot{M}(S)$ changes the sign due to the tumble of bacteria. Thus, when we denote the internal states of the bacteria moving toward (or outward) the maximum aggregation density as y^+ (or y^-), the temporal evolution of y^\pm at each instant is written as

$$\dot{y}^\pm = \pm |\partial_x M| - \frac{y}{\tau}.$$

When the adaptation time τ is much smaller than the run time λ_0^{-1} , i.e., $\lambda_0 \tau \ll 1$, the internal state is determined by the local equilibrium state as $y^\pm = \pm \tau |\partial_x M|$ in each run duration.

On the other hand, at the large relative adaptation time $\alpha = 100$ (i.e., Figs. 5(a) and 6(a)), the both distributions f_r^\pm concentrate around $y = 0$ in the scaled internal variable $y/(\tau G)$, while at the moderate relative adaptation time $\alpha = 1$ (i.e., Figs. 5(b) and 6(b)), the internal state moderately concentrates around $y_p^\pm = \pm \tau |\partial_x M|$ at each local position r .

These behaviors of the internal state variable y according to the change of the relative adaptation time α are consistent with the continuum-limit solutions obtained by the asymptotic analysis, which is presented in the next section and also in Ref. [20]; that is, the continuum limit solution at $\lambda_0^{-1} \rightarrow 0$ is obtained as $f_0^\pm(t, x, y) = \rho(t, x) \delta(\frac{y}{\tau} = \pm \partial_x M(S))$ when $\alpha \ll 1$ and $f_0^\pm(t, x, y) = \rho(t, x) \delta(y = 0)$ when $\alpha \gg 1$. When $\alpha = 1$, the distribution of the internal state moderately concentrates around $y = \pm \tau \partial_x M(S)$. It is also seen that this characteristic behavior of the internal state variable with respect to the relative adaptation time α is less affected by the change of the stiffness parameter δ being compared to the dependency of the macroscopic population density ρ on the stiffness parameter δ . In the next subsection, we consider how the stiffness parameter δ affects the individual motions of bacteria to create different aggregation profiles shown in Figs. 1 and 2.

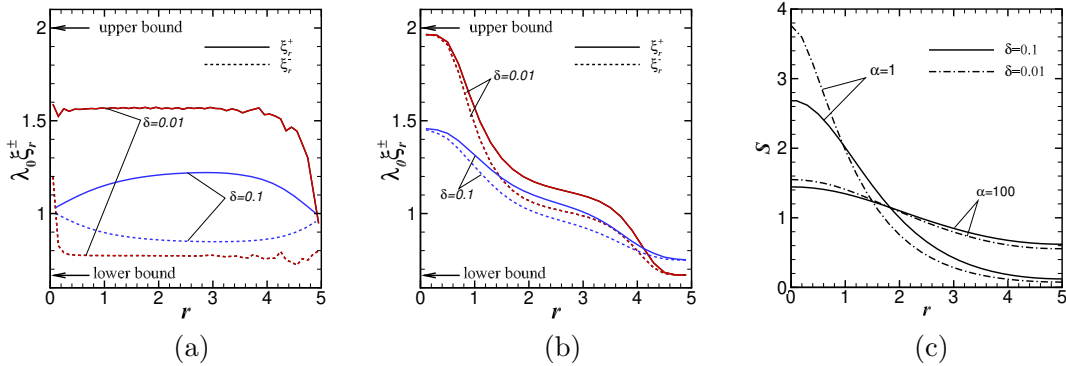


FIGURE 7. Spatial distributions of the mean run length ξ_r^\pm , defined by Eq. (20), and the chemical cue S in the stationary state at different values of the stiffness parameter δ . Figure (a) and (b) show the results of the mean run length at $\alpha = 1$ and $\alpha = 100$, respectively, and Figure (c) shows the results of chemical cue at the same parameter sets. The mean tumbling frequency $\lambda_0 = 10$ is fixed.

3.2.3. *Local mean run length.* Figure 7 shows the spatial distributions of the local mean run length of bacteria at the moderate stiffness $\delta = 0.1$ and at the large stiffness $\delta = 0.01$. Here, the local mean run length ξ_r^\pm is calculated as

$$\xi_r^\pm = \int \frac{f_r^\pm(y)}{\rho_r \lambda_0 \Lambda(\frac{y}{\delta})} dy, \quad (20)$$

where ρ_r is the population density at the distance r . Thus, ξ_r^+ denotes the local mean run length of the bacteria moving toward the maximum aggregation density at the distance r while ξ_r^- denotes that of the bacteria moving outward the maximum aggregation density at the distance r . Since the modulation function $\Lambda_\delta(y)$, which is defined by Eq. (6), is bounded, the mean run length is also bounded. In Figs. 7 (a) and (b), the upper and lower bounds of the mean run length are shown by leftward arrows on the vertical axis.

At the moderate relative-adaptation time $\alpha = 1$ (Fig. 7(a)), there is a significant difference between ξ_r^+ and ξ_r^- . This indicates that the bacteria create highly biased motions according to the moving directions. At the moderate stiffness $\delta = 0.1$, the biased motion is maximized around the location of the maximum gradient of $M(S)$, i.e., $|\partial_x M(S)| = |\partial_x S/S|$ (See Fig. 7(c)) while at the large stiffness $\delta = 0.01$, the biased motion is further enhanced over the whole domain except the vicinities at $r = 0$ and $r = 5$, so that the spike-like aggregation profile form due to the highly biased motions of bacteria (see also Fig. 2(b)).

On the other hand, at the large relative adaptation time $\alpha = 100$, both ξ_r^+ and ξ_r^- vary similarly according to the local amplitude (not the spatial gradient) of the chemical cue S , and so the biased motion of bacteria is less prominent. This observation is consistent with the y distributions in Figs. 5(c) and 6(c), where the difference between f_r^+ and f_r^- is small. Thus, the aggregation is weakened compared to that at the moderate relative adaptation time $\alpha = 1$.

On the contrary to the results at $\alpha=1$ [Fig. 7(a)], at $\alpha=100$ [Fig. 7(b)], the stiffness of the chemotactic response δ does not enhance the biased motions in different moving directions but amplify the spatial modulation of the mean run lengths in both moving directions although the spatial profile of the chemical cue is less affected by the stiffness parameter [Fig. 7(c)]. Remarkably, at the large stiffness $\delta = 0.01$, the mean run lengths in both moving directions ξ^\pm attain to the upper and lower bounds in the vicinities at $r=0$ and 5, respectively. Thus, the biased motion is rather hindered due to the boundedness of the tumbling frequency modulation $\Lambda_\delta(y)$ in the vicinities at $r=0$ and 5 such that the plateau regimes of the trapezoidal aggregation profile in Fig. 2(c) is created.

The overall observations in the local mean run length indicate that the biased motion of bacteria is mostly determined by the relative adaptation time α while the stiffness parameter δ just amplifies the signal of the internal state in the chemotactic response function. This orthogonal effects of the relative adaptation time α and the stiffness of the chemotactic response δ produce the variety of the aggregation profile observed in Figs. 1 and 2.

4. ASYMPTOTIC ANALYSIS

4.1. **Continuum-limit equation.** In this section, we formally derive the continuum-limit equations at $\varepsilon = \lambda_0^{-1} \rightarrow 0$ under the diffusive scalings of (10) and (13), i.e.,

$$\varepsilon \partial_t f_\varepsilon^\pm \pm \partial_x f_\varepsilon^\pm + \partial_y \left\{ \left(\varepsilon \partial_t M(S_\varepsilon) \pm \partial_x M(S_\varepsilon) - \frac{y}{\tau} \right) f_\varepsilon^\pm \right\} = \pm \frac{\Lambda_\delta(y)}{2\varepsilon} (f_\varepsilon^- - f_\varepsilon^+). \quad (21)$$

$$\varepsilon \partial_t S_\varepsilon = D_S \partial_{xx} S_\varepsilon - S_\varepsilon + \rho_\varepsilon, \quad (22)$$

We consider three different adaptation time scalings; i.e., (I) $\tau = O(\varepsilon)$ (i.e., $\alpha = O(1)$), (II) $\tau = O(\varepsilon^2)$ (i.e., $\alpha = O(\varepsilon)$), and (III) $\tau = O(1)$. Here, we set the time scaling parameters as $\sigma = \sigma_S = \varepsilon$.

In Ref. [20], the asymptotic analysis of the continuous velocity version of Eq. (13) is carried out at the same scalings of the adaptation time under the assumption that the stiffness parameter δ is the same order

as the adaptation time, i.e., $\delta = O(\tau)$, and the spatial gradient of $M(S)$ is uniform, i.e., $\nabla_x M(S) = G$ where G is constant. The results of Ref. [20] are briefly summarized as following:

- In Case I, supposed $\chi = O(\varepsilon)$, a hyperbolic model is found at $\sigma = 1$ while a novel type of the Flux-Limited KS model is found at $\sigma = \varepsilon$. Furthermore, in both time scalings ($\sigma=1$ and ε), the leading order solution f_0 is obtained from a new type of equilibrium equation (which is the continuous velocity version of Eq. (27)).
- In Case II, supposed $\chi = O(\varepsilon)$, a FLKS model is obtained at $\sigma = \varepsilon$, and the leading order solution is explicitly written as $f_0 = \rho(t, x)\delta(y = v \cdot G)$.
- In Case III, a classical KS type model is obtained for $\sigma = \varepsilon$, and the leading order solution is explicitly written as $f_0 = \rho(t, x)\delta(y = 0)$.

In this paper, we consider the case where both stiffness and modulation are moderate, i.e., $\delta = O(1)$ and $\chi = O(1)$. By taking the sum of Eq. (21), we have

$$\partial_t \left(\frac{f_\varepsilon^+ + f_\varepsilon^-}{2} \right) + \partial_x \left(\frac{f_\varepsilon^+ - f_\varepsilon^-}{2\varepsilon} \right) + \partial_y \left\{ \left(\varepsilon \partial_t M_\varepsilon - \frac{y}{\tau} \right) \left(\frac{f_\varepsilon^+ + f_\varepsilon^-}{2} \right) + \partial_x M_\varepsilon \left(\frac{f_\varepsilon^+ - f_\varepsilon^-}{2\varepsilon} \right) \right\} = 0.$$

By integrating the above equation with respect to y , we obtain

$$\partial_t \rho_\varepsilon + \partial_x \left(\frac{J_\varepsilon}{\varepsilon} \right) = 0, \quad (23)$$

where the flux J_ε is defined as

$$J_\varepsilon = \int_R \frac{f_\varepsilon^+ - f_\varepsilon^-}{2} dy. \quad (24)$$

The continuum-limit equations for the population density ρ_0 can be derived from the above formulas (23) and (24).

By taking the continuum limit at Eq. (22), S_0 is described by the following equation;

$$-D_S \partial_{xx} S_0 + S_0 = \rho_0. \quad (25)$$

4.1.1. *Case I:* $\tau = O(\varepsilon)$. By changing the variable as $z = \frac{y}{\tau}$, Eq. (21) is written as

$$\varepsilon^2 \partial_t f_\varepsilon^\pm \pm \varepsilon \partial_x f_\varepsilon^\pm + \frac{1}{\alpha} \partial_z \left\{ (\varepsilon \partial_t M_\varepsilon \pm \partial_x M_\varepsilon - z) f_\varepsilon^\pm \right\} = \pm \frac{\Lambda_\delta(\varepsilon \alpha z)}{2} (f_\varepsilon^- - f_\varepsilon^+), \quad (26)$$

where α is the relative adaptation time introduced in Sec. 3.2, i.e., $\alpha = \tau/\varepsilon$. We note that $\Lambda_\delta(\varepsilon \alpha z) = 1 - R_\delta(\varepsilon \alpha z)$ and $|R_\delta(\varepsilon \alpha z)| \leq \frac{\varepsilon \alpha |z|}{\delta}$. Thus, from the leading term, we can formally obtain

$$\partial_z [(\pm G_0 - z) f_0^\pm] = \pm \frac{\alpha}{2} (f_0^- - f_0^+),$$

where we write $G_0 = \partial_x M_0$. Here, we assume that f_ε^\pm is compactly supported with respect to y . (This can be proved when $|G_0|$ is bounded as is done in Sec. 3 of Ref. [20].) By integrating the above equation with respect to z , we obtain $J_0 = 0$.

We seek the leading-order solution in the form of $f_0^\pm = \rho_0(t, x) Q_0^\pm(z; G_0)$, where Q_0^\pm is described as

$$\partial_z [(\pm G_0 - z) Q_0^\pm] = \pm \frac{\alpha}{2} (Q_0^- - Q_0^+), \quad (27)$$

with $\int_R Q_0^\pm dz = 1$. In Ref. [20], the existence and uniqueness of the continuous velocity version of Eq. (27) for a given G_0 is proved. Furthermore, Q_0^\pm is compactly supported on $y = [-|G_0|, |G_0|]$.

With using the leading order solution, we can write Eq. (26) as

$$\begin{aligned} & \pm \partial_x (\rho_0 Q_0^\pm) + \frac{1}{\alpha} \partial_z \left\{ \partial_t M_0 \rho_0 Q_0^\pm + (\pm G_0 - z) f_1^\pm \right\} \\ & = \pm \frac{1}{2} (f_1^- - f_1^+) \pm \frac{\alpha \chi \rho_0}{2\delta} z (Q_0^+ - Q_0^-) + O(\varepsilon), \end{aligned}$$

where we use $R_\delta(\varepsilon\alpha z) = \frac{\varepsilon\alpha z}{\delta} + O(\varepsilon^2)$ for $z \in [-|G_0|, |G_0|]$. By integrating the above equation with respect to z and taking the limit $\varepsilon \rightarrow 0$, we obtain

$$J_1 = \partial_x \rho_0 - \frac{\alpha\chi\rho_0}{2\delta} \int_{-|G|}^{|G|} z(Q_0^+ - Q_0^-) dz.$$

Here, we also assume $\int_R |z(f_1^- - f_1^+)| dz < +\infty$. The last term of the above equation is calculated as following; By integrating Eq. (27) multiplied by z , we have

$$\begin{aligned} \int z \partial_z [(\pm G - z)Q_0^\pm] dz &= \pm \frac{\alpha}{2} \int z(Q_0^- - Q_0^+), \\ - \int (\pm G - z)Q_0^\pm dz &= \pm \frac{\alpha}{2} \int z(Q_0^- - Q_0^+), \\ \mp G + \int zQ_0^\pm dz &= \pm \frac{\alpha}{2} \int z(Q_0^- - Q_0^+), \\ \int z(Q_0^+ - Q_0^-) dz &= \frac{2G}{1+\alpha}. \end{aligned}$$

Thus, we obtain

$$J_1 = \partial_x \rho_0 - \frac{\alpha\chi G\rho_0}{\delta(1+\alpha)}.$$

Hence, from Eq. (23), we obtain the following KS equation in the continuum limit $\varepsilon \rightarrow 0$,

$$\partial_t \rho_0 - \partial_{xx} \rho_0 + \partial_x \left(\frac{\alpha\chi \partial_x M(S_0)}{\delta(1+\alpha)} \rho_0 \right) = 0. \quad (28)$$

4.1.2. *Case II: $\tau = O(\varepsilon^2)$.* By setting $\alpha = \alpha_1 \varepsilon$ at Eq. (26), we have

$$\varepsilon^2 \partial_t f_\varepsilon^\pm \pm \varepsilon \partial_x f_\varepsilon^\pm + \frac{1}{\alpha_1 \varepsilon} \partial_z \{ (\varepsilon \partial_t M_\varepsilon \pm \partial_x M_\varepsilon - z) f_\varepsilon^\pm \} = \pm \frac{\Lambda_\delta(\varepsilon^2 \alpha_1 z)}{2} (f_\varepsilon^- - f_\varepsilon^+). \quad (29)$$

From the leading term of the above equation, we obtain

$$\partial_z [(\pm \partial_x M_0 - z) f_0^\pm] = 0.$$

Thus, the leading order solution is written as

$$f_0^\pm = \rho_0 \delta(z = \pm \partial_x M_0), \quad (30)$$

where $\delta(z)$ is Dirac delta function. The leading order flux is obtained as $J_0 = 0$.

By taking the difference of Eq. (29) and integrating it with respect to z , we obtain

$$\varepsilon \partial_x \rho_\varepsilon = -J_\varepsilon + \int_R \frac{R_\delta(\varepsilon^2 \alpha_1 z)}{2} (f_\varepsilon^- - f_\varepsilon^+) dz + O(\varepsilon^2).$$

By taking the limit $\varepsilon \rightarrow 0$ of the above equation under the assumption $\int_R |z(f_\varepsilon^- - f_\varepsilon^+)| dz < +\infty$, we obtain

$$J_1 = -\partial_x \rho_0.$$

Hence, from Eq. (23), we obtain the following diffusion equation at the continuum limit $\varepsilon \rightarrow 0$,

$$\partial_t \rho_0 - \partial_{xx} \rho_0 = 0. \quad (31)$$

It should be noted that this equation coincides with Eq. (28) at the limit $\alpha \rightarrow 0$.

4.1.3. *Case III: $\tau = O(1)$.* The leading term of Eq. (21) gives us

$$f_0^+ = f_0^- = f_0, \quad (32)$$

and hence, $J_0 = 0$.

Thus, the next order term is written as

$$\pm \partial_x f_0 + \partial_y \left\{ \left(\pm \partial_x M_0 - \frac{y}{\tau} \right) f_0 \right\} = \pm \frac{\Lambda_\delta(y)}{2} (f_1^- - f_1^+). \quad (33)$$

By taking the sum of the above equation, we obtain

$$\partial_y(yf_0) = 0.$$

Hence, the leading order solution is written as

$$f_0 = \rho_0(t, x)\delta(y = 0). \quad (34)$$

Thus, from Eq. (33) with Eq. (34), the flux J_1 is calculated as

$$\begin{aligned} J_1 &= - \int \frac{\delta(y = 0)}{\Lambda_\delta(y)} dy \partial_x \rho_0 - \rho_0 \partial_x M_0 \int \frac{\delta'(y = 0)}{\Lambda_\delta(y)} dy, \\ &= - \frac{1}{\Lambda_\delta(0)} \partial_x \rho_0 + \frac{\Lambda'_\delta(0)}{\Lambda_\delta^2(0)} \rho_0 \partial_x M_0. \end{aligned}$$

Since $\Lambda_\delta(0) = 1$ and $\Lambda'_\delta(0) = \frac{\chi}{\delta}$, we obtain

$$J_1 = -\partial_x \rho_0 + \frac{\chi \rho_0 \partial_x M_0}{\delta}, \quad (35)$$

and hence,

$$\partial_t \rho_0 - \partial_{xx} \rho_0 + \partial_x \left(\frac{\chi \partial_x M_0}{\delta} \rho_0 \right). \quad (36)$$

It should be noted that this equation coincides with Eq. (28) at the limit $\alpha \rightarrow \infty$.

4.2. Linear instability of the KS system. In the previous section, we show that for a moderate stiffness $\delta = O(1)$, we uniformly obtain the KS equation (28) at the continuum limit $\varepsilon = \lambda^{-1} \rightarrow 0$ even at the different scalings of the adaptation time. The linear instability of the KS system around the uniform solution $\rho = S = 1$ is obtained as following:

First, we consider a small perturbation of the uniform solution in the following form,

$$\rho(t, x) = 1 + \tilde{\rho}(x)e^{\mu t}, \quad S(t, x) = 1 + \tilde{S}(x)e^{\mu t},$$

and linearize Eq. (28) as

$$\begin{aligned} \mu \tilde{\rho}(x)e^{\mu t} - \tilde{\rho}''(x)e^{\mu t} + \partial_x \left(\frac{\alpha \Lambda'_\delta(0)}{1 + \alpha} \tilde{S}'(x)e^{\mu t} (1 + \tilde{\rho}(x)e^{\mu t}) \right) &= 0, \\ \mu \tilde{\rho}(x) - \tilde{\rho}''(x) + \left(\frac{\alpha \Lambda'_\delta(0)}{1 + \alpha} \right) \tilde{S}''(x) &= 0. \end{aligned}$$

By taking the Fourier transform of the above equations, we obtain

$$\mu \tilde{\rho}_k + k^2 \left(\tilde{\rho}_k - \frac{\alpha \Lambda'_\delta(0)}{1 + \alpha} \tilde{S}_k \right) = 0, \quad (37)$$

where k is the Fourier variable and $\tilde{\rho}_k$ and \tilde{S}_k are the Fourier transform of $\tilde{\rho}(x)$ and $\tilde{S}(x)$, respectively, which are calculated as $\tilde{\rho}_k = \int_{\mathbb{R}} \tilde{\rho}(x) e^{-ikx} dx$. By inserting the Fourier transform of Eq. (25),

$$\begin{aligned} (1 + D_S k^2) \tilde{S}_k &= \tilde{\rho}_k, \\ \tilde{S}_k &= \frac{\tilde{\rho}_k}{1 + D_S k^2}, \end{aligned}$$

into Eq. (37), we obtain

$$\left[\mu + k^2 \left(1 - \frac{\alpha \Lambda'_\delta(0)}{(1+\alpha)(1+D_S k^2)} \right) \right] \tilde{\rho}_k = 0. \quad (38)$$

Hence, the condition that the mode k becomes linearly unstable ($\mu > 0$) is written as

$$\Lambda'_\delta(0) > \frac{1+\alpha}{\alpha} (1 + D_S k^2). \quad (39)$$

Thus, the instability of the mode k occurs when the stiffness of the chemotactic response $\Lambda'_\delta(0)$ is larger than the right-hand side of Eq. (39). This also indicates that when the stiffness of the response $\Lambda'_\delta(0)$ and the diffusion coefficient D_S are fixed, the instability more likely occurs as α increases.

4.3. Asymptotic behavior. In this section, we further discuss about the asymptotic behavior of the population density with respect to $\varepsilon = \lambda_0^{-1}$ at large adaptation times; i.e., (i) $\tau = O(1)$ and (ii) $\tau = O(\lambda_0)$. Figure 8 shows the asymptotic behaviors of the population density at the moderate stiffness $\delta = 0.1$. It is

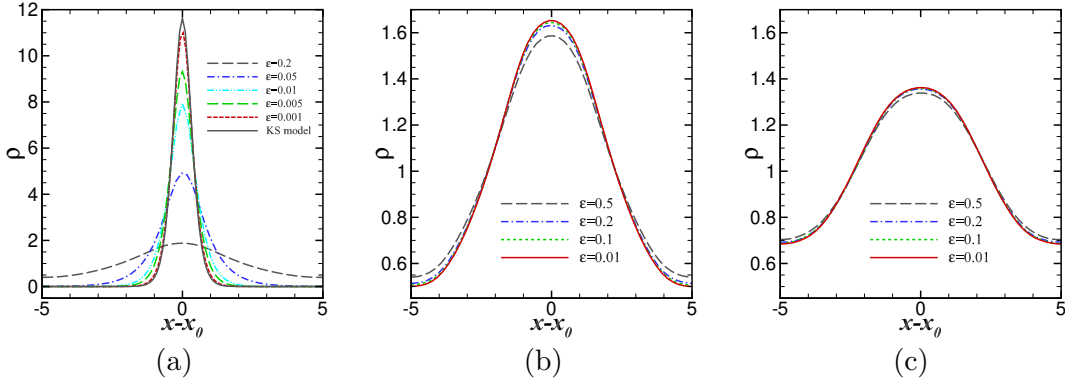


FIGURE 8. Asymptotic behaviors of the population density ρ at the moderate stiffness $\delta = 0.1$. Figure (a), (b), and (c) show the results at different scalings of the adaptation time, i.e., $\tau = 1$, $\tau = 1/\varepsilon$, and $\tau = 2/\varepsilon$, respectively. Here, ε is defined as $\varepsilon = \lambda_0^{-1}$.

seen that at $\tau = 1$, the MC results approach to that of the KS system as ε decreases. This observation is consistent with the asymptotic analysis in Sec. 4.1.3. However, the asymptotic convergence is very slow; a significant deviation remains between MC results and KS system even at small ε , say $\varepsilon \sim 0.01$.

This slow asymptotic convergence is also confirmed in Fig. 4, where the MC results at $\tau = 1$ line up in an upper-right direction and they gradually approach to the KS limit as the relative adaptation time α increases. On the other hand, it is also seen that, when α is fixed at $\alpha = O(1)$, i.e., $\tau = O(\varepsilon)$, the MC results converge to the KS result more rapidly as ε decreases.

When the adaptation time is set as $\tau = \tau_\varepsilon/\varepsilon$ (e.g., $\tau_\varepsilon=1$ at Fig. 8(b) and $\tau_\varepsilon=2$ at Fig. 8(c)), the asymptotic convergence of the MC results is much faster at $\tau = O(1/\varepsilon)$ compared to that observed at $\tau = 1$; even at moderately small ε , say $\varepsilon \sim 0.1$, the MC results numerically converge to that obtained at $\varepsilon = 0.01$. It is also seen that the numerical solutions are significantly affected by the change of τ_ε . This seems to indicate that some robust asymptotic solution exists at $\tau = O(1/\varepsilon)$, and that the relevant parameter regime for the KS system is restricted such that $\tau \ll \lambda_0$.

Since τ and λ_0 are nondimensionalized as Eq. (9), the restriction $\tau \ll \lambda_0$ is rewritten in the dimensional form as

$$\tau \ll t_d, \quad t_d = \frac{L_0^2}{D_\rho}, \quad (40)$$

where t_d is the diffusion time in the characteristic length L_0 and D_ρ is the diffusion constant of the macroscopic population density of bacteria defined as $D_\rho = V_0^2/\lambda_0$. Thus, the asymptotic behavior of the MC results says that the KS model is only valid when the adaptation time τ is much smaller than the diffusion time of the macroscopic population density t_d , and that a novel asymptotic solution may exist at the large adaptation time scaling $\tau = O(t_d)$.

It should be also noted that the maximum aggregation density decreases as τ_ε increases. This behavior is also confirmed from Fig. 4. Thus, the nonmonotonic behavior of the maximum aggregation density with respect to the adaptation time τ at each fixed ε can be viewed as the transition from the KS-type solution to a certain asymptotic solution which may exist at $\tau = O(1/\varepsilon)$.

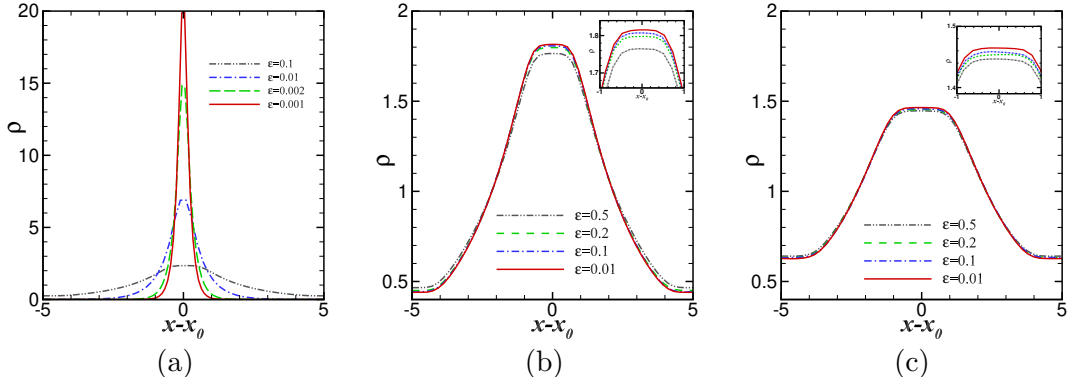


FIGURE 9. Asymptotic behaviors of the population density ρ at the large stiffness $\delta = 0.01$. Figure (a), (b), and (c) show the results at different scalings of the adaptation time, i.e., $\tau = 5$, $\tau = 1/\varepsilon$, and $\tau = 2/\varepsilon$, respectively. The inset show the magnification around the center of the aggregation.

Figure 9 shows the asymptotic behaviors of the population density at the large stiffness $\delta = 0.01$. It is seen from Fig. 9(a) that when $\tau = 5$ is fixed, the width of the aggregation is narrower and narrower as ε is smaller and smaller, so that the asymptotic convergence is not confirmed from the present MC results.

Interestingly, the trapezoidal aggregation is robustly formed at $\tau = O(\lambda_0)$; in Figs. 9(b) and (c), the MC results at moderately small ε , say $\varepsilon \lesssim 0.1$, are close to each other and asymptotically converge to a trapezoidal profile, which is also observed in Fig. 2. This seems to indicate that the trapezoidal aggregation is related to the novel asymptotic solution which may exists at $\tau = O(\lambda_0)$ at the large stiffness (although it is not confirmed yet). The asymptotic analysis at the large adaptation time scaling will be important future work.

5. SUMMARY AND PERSPECTIVES

We have investigated the self-organized aggregations of chemotactic cells in one-dimensional space with periodic boundary conditions based on a two-stream kinetic transport model with an internal state coupled with the chemoattractant equation. Monte Carlo simulations were conducted for a wide range of adaptation times τ at various values of the mean tumbling frequency λ_0 and stiffness δ .

We found that the aggregation behavior is highly affected by the adaptation time τ ; the instability diagram and the dependency of the maximum aggregation density on the adaptation time are shown in Figs. 3 and 4, respectively, where we introduce the new parameter defined by the ratio of the adaptation time to the mean run time, i.e., the relative adaptation time $\alpha = \lambda_0\tau$. A sharp transition between stable and unstable modes is observed in the small relative adaptation time regime, $\alpha \lesssim 1$, where instability always occurs when

the relative adaptation time α is slightly larger than the critical value calculated by the linear instability condition of the KS model derived from the kinetic transport model in the continuum limit.

However, in the large α regime, $\alpha = O(\lambda_0)$, the MC results deviate from the linear stability analysis of the KS model even at small $\varepsilon = \frac{1}{\lambda_0}$, $\varepsilon \sim 0.01$, where the maximum aggregation density gradually decreases as α increases, and the slope of the decrease is larger as ε is larger. Thus, there exists an optimal adaptation time to enhance the aggregation behavior around $1 \lesssim \alpha \ll \lambda_0$. This nonmonotonic behavior is a significantly important feature that can be described at the kinetic level but not at the KS level; in the KS model, the maximum aggregation density monotonically increases and saturates to a certain value as α increases.

We also sought to characterize the variety of aggregation profiles in Figs. 1 and 2 from a microscopic point of view; Figs. 5 and 6 show the local distributions of the internal state, and Fig. 7 shows the spatial distribution of the local mean run length. Here, we found orthogonal effects of the adaptation time τ and the stiffness of the chemotactic response δ on the microscopic dynamics. That is, the adaptation time τ significantly affects the distribution of the internal state, while the stiffness δ does not similarly affect the distribution of the internal state but only amplify enhance the signal of the internal state in the response function $R_\delta(y)$ such that the characteristic features of individual motions of bacteria, i.e., the local mean run length, at each adaptation time is enhanced.

When the relative adaptation time is moderate, $\alpha = O(1)$, individual cells exhibit highly biased motion depending on the moving direction, and the biased motion is enhanced at the large stiffness $\delta = 0.01$ such that the spike-like aggregation profile observed in Fig. 2(b) is produced. On the other hand, when the relative adaptation time is large, $\alpha = O(\lambda_0)$, the biased motion is hindered, but the mean run length grows with the concentration of the chemical cue S (not with the gradient of S). Furthermore, at a large stiffness, the mean run length attains the upper and lower bounds due to the boundedness of the modulation function $\Lambda_\delta(y)$ near the center and edges of the aggregation profile, where the aggregation is hindered such that the trapezoidal aggregation profile observed in Fig. 2(c) is produced.

Finally, we also found very interesting asymptotic behavior of the aggregation density at large adaptation times, as shown in Figs. 8 and 9. The asymptotic behavior of the MC results reveals that the appropriate parameter regime for the classical KS system is restricted such that the adaptation time is much smaller than the diffusion time of macroscopic population density [Eq. (40)], and that the trapezoidal aggregation profile is robustly formed at the large adaptation time scaling of $\tau = O(\lambda_0)$. Furthermore, the MC results seem to indicate that a novel type of asymptotic solution may exist at the large adaptation time regime. The asymptotic solution at the large adaptation time scaling will be an important future study.

One may think that such a large adaptation time is biologically unrealistic. However, when the system size is as small as $L_0 \sim 100 \mu\text{m}$ and the mean run length of bacteria is measured as $l_0 \sim 20 \mu\text{m}$, the ratio of the mean run length of bacteria to the system size, ε is typically estimated as $\varepsilon \sim 0.2$, so the relative adaptation time is estimated as $\alpha \sim 25$ at the large adaptation time scaling. The adaptation time of bacteria is usually much longer than the run time, so $\alpha \sim 25$ is not unrealistic but rather commonly observed. Indeed, when the system size is as small as $\varepsilon \sim 0.1$, unusual aggregation behaviors of bacteria are observed in experiments. For example, in Ref. [18], the volcano-like aggregation profile of *E. coli* is observed at $L_0 \sim 100 \mu\text{m}$, and in Ref. [1], swarm bands of marine bacteria around a chemoattractant microbead with a distance of approximately $L_0 \sim 20 \mu\text{m}$ are observed. The common feature in these curious aggregation behaviors is that the maximum aggregation density is not located at the center of the aggregation but rather at a certain distance from the center. It is interesting that the trapezoidal aggregation profile is obtained in the present MC simulation in the same parameter regime as in the experiments, although neither volcano-like aggregation nor swarm rings have yet been confirmed.

In the present kinetic transport model, we utilize the simplified model for intracellular signal transduction in which only the adaptation dynamics of the internal state are considered while the excitation dynamics, which are much faster than the adaptation dynamics, are ignored. We also consider the velocity-jump kinetic model, in which the tumbling time (i.e., the time required for the bacteria to change their moving direction) is ignored since it is much shorter than the run time. In small-size systems, these fast-time-scale dynamics may bring about a delay in individual motion and affect the collective dynamics. Indeed, in the literature [2, 11, 27], the nonunimodal aggregations around a chemoattractant point source are numerically reproduced by using a model involving either the excitation dynamics of the internal state or the tumbling time.

Recently, it has also been reported that the noise arising in the intracellular signal transduction process plays a significant role in the occurrence of chemotactic aggregation around a chemoattractant point source[4] and even in the fractional diffusion mode in the collective motion of bacteria[24,30]. To uncover the instability conditions and the parameter regimes for the variety of aggregation behaviors, further investigations based on the kinetic transport model involving more sophisticated formulas of the intracellular signal transduction pathway and the tumbling state will be important future work.

REFERENCES

- [1] Greg M. Barbara and James G. Mitchell, *Marine bacterial organisation around point-like sources of amino acids*, FEMS Microbiology Ecology **43** (2003), no. 1, 99–109.
- [2] D. Bray, M.D. Levin, and K. Lipkow, *The chemotactic behavior of computer-based surrogate bacteria*, Current Biology **17** (2007), no. 1, 12–19.
- [3] Douglas A. Brown and Howard C. Berg, *Temporal stimulation of chemotaxis in escherichia coli*, Proceedings of the National Academy of Sciences **71** (1974), no. 4, 1388–1392.
- [4] Douglas R. Brumley, Francesco Carrara, Andrew M. Hein, Yutaka Yawata, Simon A. Levin, and Roman Stocker, *Bacteria push the limits of chemotactic precision to navigate dynamic chemical gradients*, Proceedings of the National Academy of Sciences **116** (2019), no. 22, 10792–10797.
- [5] E. Budrene and H. Berg, *Complex patterns formed by motile cells of Escherichia coli*, Nature **349** (1991), 630–633.
- [6] V. Calvez, B. Perthame, and S. Yasuda, *Traveling wave and aggregation in a flux-limited keller-segel model*, Kinetic and Related Models **11** (2018), no. 4, 891–909.
- [7] Y. Dolak and C. Schmeiser, *Kinetic models for chemotaxis: Hydrodynamic limits and spatio-temporal mechanisms*, J. Math. Biol. **51** (2005), 595–615.
- [8] R. Erban and H. Othmer, *From individual to collective behaviour in bacterial chemotaxis*, SIAM J. Appl. Math. **65** (2004), no. 2, 361–391.
- [9] R. Erban and H. Othmer, *Taxis equations for amoeboid cells*, J. Math. Biol. **54** (2007), 847–885.
- [10] T. Hillen and K. J. Painter, *A user’s guide to pde models for chemotaxis*, J. Math. Biol. **58** (2009), 183–217.
- [11] Gregory Javens, Hossein Jashnsaz, and Steve Pressé, *From the volcano effect to banding: a minimal model for bacterial behavioral transitions near chemoattractant sources*, Physical Biology **15** (2018), no. 4, 046002.
- [12] L. Jiang, Q. Ouyang, and Y. Tu, *Quantitative modeling of escherichia coli chemotactic motion in environments varying in space and time*, PLoS Computational Biology **6** (2010), no. 4.
- [13] Y.V. Kalinin, L. Jiang, Y. Tu, and M. Wu, *Logarithmic sensing in escherichia coli bacterial chemotaxis*, Biophys J. **96** (2009), no. 6, 2439–2448.
- [14] E. F. Keller and L. A. Segel, *Model for chemotaxis*, J. Theor. Biol. **30** (1971), 225–234.
- [15] E.F. Keller and L.A. Segel, *Initiation of slime mold aggregation viewed as an instability*, J. Theor. Biol. **26** (1970), 399–415.
- [16] Hazelbauer G. L., *Bacterial chemotaxis: the early years of molecular studies*, Annu. Rev. Microbiol **66** (2012), 285–303.
- [17] Chenli Liu, Xiongfei Fu, Lizhong Liu, Xiaojing Ren, Carlos K.L. Chau, Sihong Li, Lu Xiang, Hualing Zeng, Guanhua Chen, Lei-Han Tang, Peter Lenz, Xiaodong Cui, Wei Huang, Terence Hwa, and Jian-Dong Huang, *Sequential establishment of stripe patterns in an expanding cell population*, Science **334** (2011), no. 6053, 238–241.
- [18] N. Mittal, E.O. Budrene, M.P. Brenner, and A. Van Oudenaarden, *Motility of escherichia coli cells in clusters formed by chemotactic aggregation*, Proceedings of the National Academy of Sciences of the United States of America **100** (2003), no. 23, 13259–13263.

- [19] H.G. Othmer, S.R. Dunbar, and W. Alt, *Models of dispersal in biological systems*, Journal of Mathematical Biology **26** (1988), no. 3, 263–298.
- [20] B. Perthame, W. Sun, M. Tang, and S. Yasuda, *Multiple asymptotics of kinetic equations with internal states*, Mathematical Models and Methods in Applied Sciences **30** (2020), no. 06, 1041–1073.
- [21] B. Perthame, M. Tang, and N. Vauchelet, *Derivation of the bacterial run-and-tumble kinetic equation from a model with biological pathway*, J. Math. Biol. **73** (2016), 1161–1178.
- [22] B. Perthame, N. Vauchelet, and Z.A. Wang, *The flux-limited keller-segel system; properties and derivation from kinetic equations*, Revista Mathematica Iberoamericana (In press).
- [23] B. Perthame and S. Yasuda, *Stiff-response-induced instability for chemotactic bacteria and flux-limited Keller-Segel equation*, Nonlinearity **31** (2018), no. 9, 4065–4089.
- [24] Benoit Perthame, Weiran Sun, and Min Tang, *The fractional diffusion limit of a kinetic model with biochemical pathway*, ZEITSCHRIFT FÜR ANGEWANDTE MATHEMATIK UND PHYSIK **69** (2018), no. 3.
- [25] S.D. Ryan, *Role of hydrodynamic interactions in chemotaxis of bacterial populations*, Physical Biology **17** (2020), no. 1.
- [26] G. Si, T. Wu, Q. Ouyang, and Y. Tu, *pathway-based mean-field model for Escherichia coli chemotaxis*, Phys. Rev. Lett. **109** (2012), 048101.
- [27] J.E. Simons and P.A. Milewski, *The volcano effect in bacterial chemotaxis*, Mathematical and Computer Modelling **53** (2011), no. 7-8, 1374–1388.
- [28] Peter A. Spiro, John S. Parkinson, and Hans G. Othmer, *A model of excitation and adaptation in bacterial chemotaxis* **94** (1997), no. 14, 7263–7268.
- [29] W. Sun and M. Tang, *Macroscopic limits of pathway-based kinetic models for E. coli chemotaxis in large gradient environments*, Multiscale Model. Simul. **15** (2017), no. 2, 797–826.
- [30] Weiran Sun, Min Tang, and Xiaoru Xue, *Mathematical modelling and analysis of fractional diffusion induced by intracellular noise*, 2019.
- [31] Yuhai Tu, Thomas S. Shimizu, and Howard C. Berg, *Modeling the chemotactic response of escherichia coli to time-varying stimuli*, Proceedings of the National Academy of Sciences **105** (2008), no. 39, 14855–14860.
- [32] N. Vauchelet and S Yasuda, *Numerical scheme for kinetic transport equation with internal state **, 2020.
- [33] D.E. Woodward, R. Tyson, M.R. Myerscough, J.D. Murray, E.O. Budrene, and H.C. Berg, *Spatio-temporal patterns generated by salmonella typhimurium*, Biophysical Journal **68** (1995), no. 5, 2181–2189.
- [34] C. Xue, *Macroscopic equations for bacterial chemotaxis: integration of detailed biochemistry of cell signaling*, J. Math. Biol. **70** (2015), 1–44.
- [35] X. Xue, C. Xue, and M. Tang, *The role of intracellular signaling in the stripe formation in engineered escherichia coli populations*, PLoS Computational Biology **14** (2018), no. 6.
- [36] S. Yasuda, *Monte carlo simulation for kinetic chemotaxis model: An application to the traveling population wave*, Journal of Computational Physics **330** (2017), 1022–1042.

GRADUATE SCHOOL OF SIMULATION STUDIES, UNIVERSITY OF HYOGO, 650-0047 KOBE, JAPAN

Email address: yasuda@sim.u-hyogo.ac.jp